

Error mitigation for logical circuits using decoder confidence

Maria Dincă,^{1,*} Tim Chan,^{1,2,†} and Simon C. Benjamin^{1,3}

¹*Department of Materials, University of Oxford, Parks Road, Oxford OX1 3PH, United Kingdom*

²*Center for Quantum Information and Quantum Biology, The University of Osaka, 1-2 Machikaneyama, Toyonaka 560-0043, Japan*

³*Quantum Motion, 9 Sterling Way, London N7 9HJ, United Kingdom*

(Dated: January 13, 2026)

Fault-tolerant quantum computers use decoders to monitor for errors and find a plausible correction. A decoder may provide a *decoder confidence score* (DCS) to gauge its success. We adopt a *swim distance* DCS, computed from the shortest path between syndrome clusters. By contracting tensor networks, we compare its performance to the well-known *complementary gap* and find that both reliably estimate the logical error probability (LEP) in a decoding window. We explore ways to use this to mitigate the LEP in entire circuits. For shallow circuits, we just abort if any decoding window produces an exceptionally low DCS: for a distance-13 surface code, rejecting a mere 0.1% of possible DCS values improves the entire circuit's LEP by more than 5 orders of magnitude. For larger algorithms comprising up to trillions of windows, DCS-based rejection remains effective for enhancing observable estimation. Moreover, one can use the DCS to assign each circuit's output a unique LEP, and use it as a basis for maximum likelihood estimation. This can reduce the effects of noise by an order of magnitude at no quantum cost; methods can be combined for further improvements.

I. INTRODUCTION

In fault-tolerant quantum computing, we perform a series of measurements that can reveal information about the occurrence of errors on the system of qubits, without collapsing their quantum state. The set of observations generated by these measurements forms a syndrome. A key task in quantum error correction (QEC) [1, 2] is to map the syndromes observed on the error correcting code to the suspected physical error mechanisms which might have produced them, and consequently suggest plausible corrections. This process is known as decoding.

There has been recent interest in extracting more information from the decoder than just a correction; namely, an estimate of how likely it is for the most plausible correction to be actually correct. In the past, this estimate has been called ‘soft output’ [3–5] or ‘soft information’ [6–11], but we opt for the name ‘decoder confidence score’ (DCS) as it is more descriptive. It has been identified that additional information of this kind can be used in code concatenation [4, 8, 12, 13], defect identification in silicon-spin quantum processors [14], magic state distillation [15, 16] and cultivation [3, 17, 18], circuit sampling [4, 15], lattice surgery runtime reduction [10], hierarchical decoding [19, 20], and distributed quantum computing [11].

Typically, fault-tolerant quantum computing involves decoding in a series of windows: batches of syndromes collected in a finite amount of time across a small region of space are decoded at once. A typical window extent is a small multiple of the code distance [21]. The DCS is

particularly useful here, since each window can be associated with its own DCS value, thus providing a localised failure probability for each component of the quantum computation.

Two existing DCSs that have been studied for the surface code are the complementary gap and a cheaper alternative which we call the swim distance. The complementary gap was first introduced as ‘distinguishability’ in [22], before being studied further in Refs. [6, 8]. The swim distance was introduced simultaneously in Refs. [4, 15] as a faster alternative to the complementary gap (it has a lower time complexity); however, neither reference provides an accuracy comparison against the complementary gap.

In this paper, we refine the picture of the DCS with three observations. First, we use tensor network methods to compare the accuracy of the complementary gap and the swim distance under phenomenological noise. While we find the complementary gap to be somewhat more accurate, both DCSs are accurate proxies for the success probability. For the rest of the paper, we employ the swim distance as it is faster to compute. Second, we identify characteristics from the statistical distribution of the DCS that make it a useful resource for large-scale applications. Third, we explore this utility for quantum error mitigation (QEM) in logical circuits. In the case of a shallow circuit – such as logical state preparation – simply aborting when a poor DCS occurs is very effective. We then consider the case of an entire algorithm, which may involve a vast number of decoding windows. The strategy of aborting unpromising circuits remains tenable, but we find that another option is attractive: estimate the whole-circuit logical error probability using its DCS record, then perform maximum likelihood estimation (MLE) using the estimated risk. Depending on target performance, a combination of methods may be

* maria.dinca@materials.ox.ac.uk

† timothy.chan@materials.ox.ac.uk

optimal. This is shown in Fig. 7b,d as a primary result of this work.

Section II introduces the prerequisite concepts. We compare the complementary gap and the swim distance in Section III, before showing that the DCS provides rich error information for deep circuits in Section IV. Section V explores the use of the DCS in QEM and is followed by a numerical resource estimation in Section VI. We discuss limitations and future work in Section VII, then conclude in Section VIII.

II. BACKGROUND

In Section II A we discuss the role of a decoder and present the decoding problem, then in Section II B we define the DCS, the complementary gap, and the swim distance.

A. The Role of a Decoder

In this work, we focus on the surface code, for which the X and Z errors can be dealt with separately on independent decoding graphs. We consider decoding only one type (either X or Z) of error; the results for the other type of error are analogous. In error correction, nondestructive parity measurements are performed on physical qubits and the combination of their results is called the syndrome. Error chains (configurations of errors on the physical qubits) are detected only through their syndrome, but different error chains can give rise to the same syndrome. Additionally, each error chain belongs to one of two logical equivalence classes (LECs) that uniquely specifies its effect on the logical information. A decoder deduces from the syndrome a plausible LEC for the error chain that caused the syndrome.

We will mainly be concerned with decoders that deduce an explicit plausible error chain. What matters is not whether the deduced error chain equals the true error chain, but whether they belong to the same LEC. If they are in different LECs, then the decoding procedure results in a logical error. Therefore, a decoder effectively makes guesses – and while even the ideal decoder makes the best possible guess, it may nevertheless lead to a logical error. When choosing a decoder, there is a trade-off between the accuracy with which the likeliest LEC is found and the time it takes to decode.

More formally, the decoding problem involves the decoding graph $G = (V_d \cup V_b, E)$, with the set V_d of detectors and the set V_b of boundary nodes such that $V_d \cap V_b = \emptyset$. Each boundary node in V_b represents a unique boundary of the surface code (so for a memory experiment, $|V_b| = 2$). An example of how G relates to its code is shown in Fig. 1. Each edge in E represents an error mechanism that flips the one or two detectors it is incident to, and has a weight $\log_{10} \frac{1-p}{p}$ that decreases as

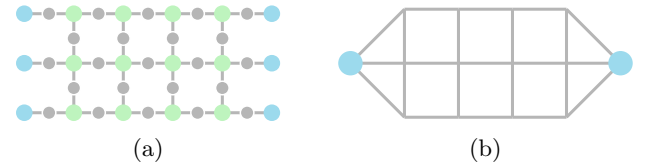


FIG. 1. (a) The X decoding graph for the $[[n, k, d_X, d_Z] = [23, 1, 5, 3]]$ unrotated surface code under code capacity noise. Detectors are green circles, boundary nodes are blue circles. In this noise model (but not necessarily in others), each detector corresponds to a Z stabiliser, and each edge corresponds to a data qubit (emphasised by a grey circle on each edge). (b) It later helps if there is only one boundary node for each unique boundary of the surface code, so we merge equivalent boundary nodes as shown. Here, we no longer show detectors nor data qubit circles.

the probability p of that error mechanism increases. Define the weight $\text{wt}(F)$ of any subset $F \subseteq E$ as the sum of the weights of all edges in that subset. The error $\mathbb{E} \subseteq E$ represents those mechanisms that actually occur, from which we define the syndrome $\mathbb{S} \subseteq V_d$ as the detectors that \mathbb{E} flips an odd number of times. Given G and \mathbb{S} , the decoder outputs a correction $\mathbb{C} = \text{DECODE}(G, \mathbb{S}) \subseteq E$ that will have the same syndrome as \mathbb{E} . We say the decoder is *successful* if \mathbb{C} is logically equivalent to \mathbb{E} .

Definition 1. The *logical error probability* (LEP), denoted p_L , is the probability that the decoder is not successful, conditioned on \mathbb{S} . The *log success odds* (or *log-likelihood ratio of success*) is given by

$$\lambda := \log_{10} \frac{1 - p_L}{p_L}. \quad (1)$$

The log success odds decreases as p_L increases. In addition to the LEP, we define the following.

Definition 2. When we have performed multiple runs of the same logical circuit, the *logical error rate* (LER) is the portion of executions with a logical error.

The LER converges to the mean LEP as the run count grows.

B. Decoder Confidence Scores

In addition to the correction, the decoder can also output the following quantity that scores how likely it believes success to be.

Definition 3. Given G and \mathbb{S} , the *DCS* is an estimator of some monotonic function $\alpha(\lambda)$ of λ . We denote its value as ϕ .

The quantity p_L (or λ) can be exactly computed by contracting a tensor network [23]; this was analysed recently in Ref. [24]. However, this method cannot be used as a real-time DCS as its time complexity is exponential. The following two definitions specify DCSs that run in polynomial time.

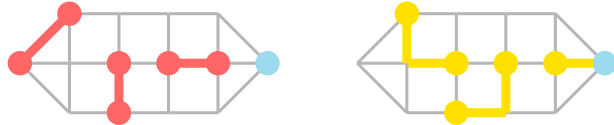


FIG. 2. Illustrating the complementary gap on the decoding graph G in Fig. 1b. The modified graph G' , shown in grey, has only one remaining boundary node, shown as a blue dot. The syndrome S (S') is the set of red (yellow) dots. The correction C (C') is the set of red (yellow) edges. The complementary gap is the weight difference between these two corrections; here it is $5 - 3 = 2$ if all edges have weight 1.

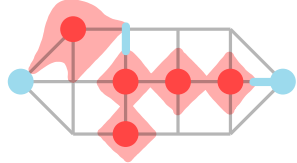


FIG. 3. Illustrating the swim distance, which is here the sum of the lengths of the blue lines: $2 \times 0.5 = 1$ if all edges have weight 1. Clusters are shaded in red.

Definition 4. The *complementary gap* is the difference in weight between the original correction and the complementary correction (the correction output by the decoder when forced to propose within the opposite LEC).

We can force the decoder to propose the opposite LEC by forcing the left boundary node to flip a number of times whose parity is opposite to that of the original correction. This is described in Algorithm 1 and illustrated by example in Fig. 2.

Algorithm 1 Pseudocode to calculate the complementary gap of a memory experiment.

```

 $\mathbb{C} \leftarrow \text{DECODE}(G, S)$ 
 $G' \leftarrow G$  but where the left boundary node  $v_L$  is a detector
 $S' \leftarrow$  the syndrome of  $\mathbb{C}$  on  $G'$ 
flip whether or not  $v_L$  is included in  $S'$ 
 $\mathbb{C}' \leftarrow \text{DECODE}(G', \mathbb{C}')$ 
return  $\text{wt}(\mathbb{C}') - \text{wt}(\mathbb{C})$ 

```

Definition 5. For any clustering decoder, the *swim distance* is the shortest path length in the decoding graph from one boundary to the other after zeroing the weights of all edges inside clusters.

Note a cluster can contain a fraction of an edge, in which case only that fraction of its weight is set to zero. Figure 3 illustrates the swim distance for the same example as in Fig. 2 and shows that its value can differ from the complementary gap. The name ‘swim distance’ is based on the following analogy: the decoding graph is a river, the two boundaries are riverbanks, and each cluster is an island in the river; then, the swim distance is the shortest distance one must swim to cross the river.

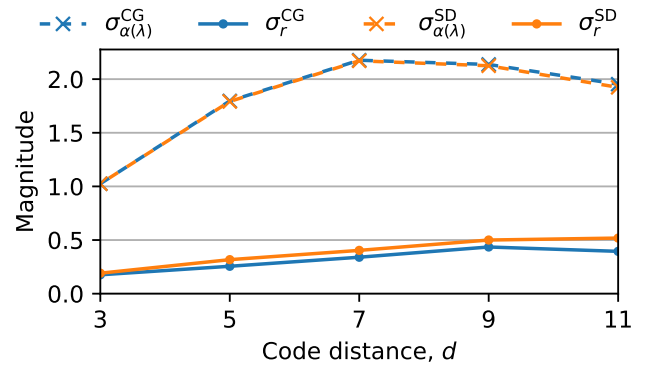


FIG. 4. The two sources of variation for the complementary gap (blue data) and the swim distance (orange data). The first source $\sigma_{\alpha(\lambda)}$ is due to the variation of the log success odds. The second source σ_r comes from the approximate nature of the DCS. Results are obtained using the MWPM decoder on the unrotated surface code under a perturbed phenomenological noise model (described in Section A 1).

The complementary gap and the swim distance are not the only DCSs that exist. For instance, Ref. [25] consider simply the weight of the original correction, Ref. [5] defines two families of scores based on how much of the decoding graph is covered by clusters, and Ref. [26] defines a score based on $|S|$ alone. Nevertheless, the complementary gap remains considerably more effective at reducing the LER in abort protocols [5]. We choose to analyse the complementary gap for this reason, and the swim distance because it has a very strong theoretical motivation [4]. For the numerics in this paper, we decode using the PyMatching implementation [27] of MWPM, calculate the complementary gap using a custom implementation, and calculate the swim distance using the implementation provided by Ref. [3].

III. DECODER CONFIDENCE SCORES ARE AN EXCELLENT INDICATOR OF LOGICAL ERROR RISK

In this section we verify that both the complementary gap and the swim distance are accurate enough to be useful in error mitigation; this is formalised as follows. The log success odds λ can be modelled as a random variable whose variation throughout a typical quantum calculation is characterised by its standard deviation σ_λ . Since the DCS ϕ is an inexact estimator of $\alpha(\lambda)$, it can be modelled as

$$\phi = \alpha(\lambda) + r, \quad (2)$$

where r is another random variable whose standard deviation σ_r represents the DCS inaccuracy. For ϕ to be useful, it must be able to resolve variations in λ between different decoding instances, i.e., $\sigma_{\alpha(\lambda)} = \alpha'(\lambda)\sigma_\lambda$ must be large compared to σ_r . Figure 4 shows this is indeed

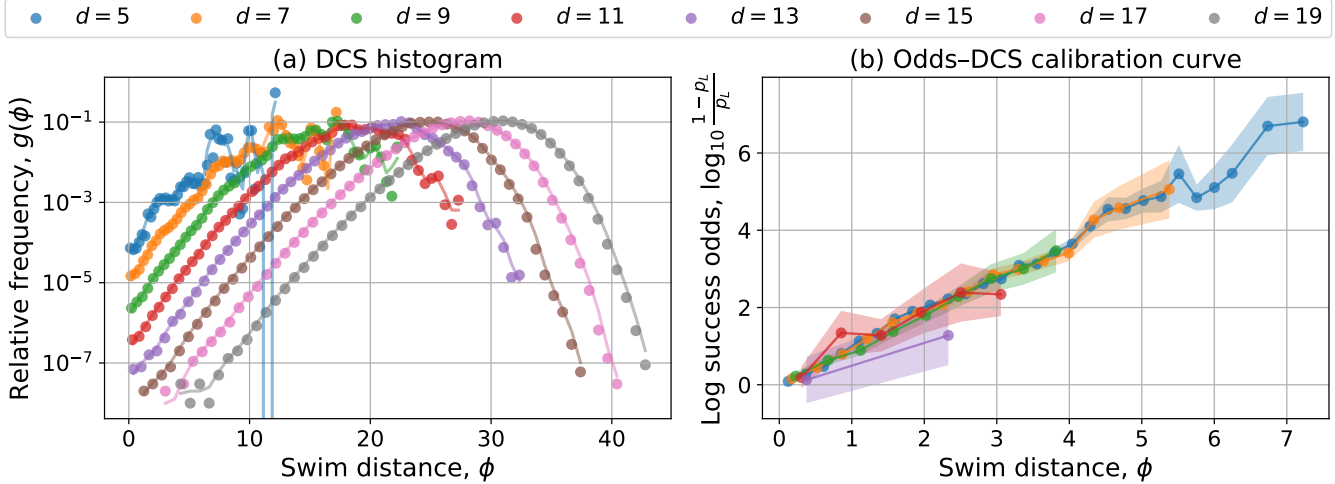


FIG. 5. **Single-decoding-window statistics.** (a) Histograms of the DCS (swim distance) value ϕ , normalised by number of shots. Under circuit-level noise, 10^8 memory experiments were run for all code distances. The ϕ values are grouped in 50 bins of equal linear width. (b) The log success odds conditioned on ϕ , plotted against ϕ . The upper and lower bounds on the Bernoulli variable p_L are given by the Wilson score interval. Only datapoints with $p_L > 0$ are shown.

the case, for both the complementary gap and the swim distance. Across all code distances considered, the complementary gap has a somewhat smaller value of $\sigma_r/\sigma_{\alpha(\lambda)}$ than the swim distance, which suggests it is a more accurate DCS. Section A describes how we obtained these quantities from our simulations.

While σ_r is smaller than $\sigma_{\alpha(\lambda)}$, it is not much smaller. The question of imperfect calibration arises: what is the effect of the DCS inaccuracy on the (early) fault-tolerant applications presented in the next sections? Answering this would require calculating the log success odds for higher code distances under a more realistic noise model than that used in Fig. 4, but we were unable to do so due to numerical imprecision during tensor network contraction. In Section V C, we provide a speculative analysis of the DCS uncertainty under a range of assumptions.

IV. DECODER CONFIDENCE SCORE DISTRIBUTIONS ARE RICH IN INFORMATION

In this section, we explore statistical properties of the DCS distribution which make it a valuable resource for error mitigation at both the single-window level, in Section IV A, and the full-application level, in Section IV B. Throughout the rest of this paper, we focus on the swim distance DCS, and we will henceforth generally refer to it as ‘the DCS’ and its value as ϕ . We will refer to single-window LEPs and logical errors by lowercase symbols (p_L, x) and to their multi-window counterparts by uppercase symbols (P_L, X). We emulate circuits using Stim [28] and assume circuit-level noise with a physical error rate $p_{\text{phys}} = 10^{-3}$. Our approach to estimating

DCS performance in the context of full logical circuits is based on allocating a suitable number of decoding windows. We do not adjust according to e.g. the specific decoding needs of logical gates, leaving that for future studies.

A. Single-Decoding-Window Statistics

We emulated memory experiments in the rotated surface code for odd code distances $d \in \{5, \dots, 19\}$; these assess how well one logical qubit stays free from logical error after d stabiliser measurement cycles. We decode each experiment in a single window and calculate ϕ for that window. The distribution of ϕ is shown in Fig. 5a. Each bin in this histogram contains a number of failed experiments (where a logical error occurred) and successful (i.e. error-free) experiments, which we use to calculate an empirical log success odds from Eq. (1). Figure 5b plots this empirical log success odds against ϕ . By fitting a straight line to this data, we obtain a calibration curve that assigns a LEP p_L to each ϕ value. These curves can be used in future experiments for the same code distance and noise model.

Despite having clear peaks, the single-window distributions in Fig. 5a provide a wide variety of LEPs if enough shots are taken. Even in the very early fault-tolerant era, the implementation of a quantum algorithm that is both useful and feasible involves a few hundred logical qubits and thousands of logical operation layers, which translates to millions of decoding windows. As technology matures further this number will rise steeply. In the next subsection we consider the total LEP of an experi-

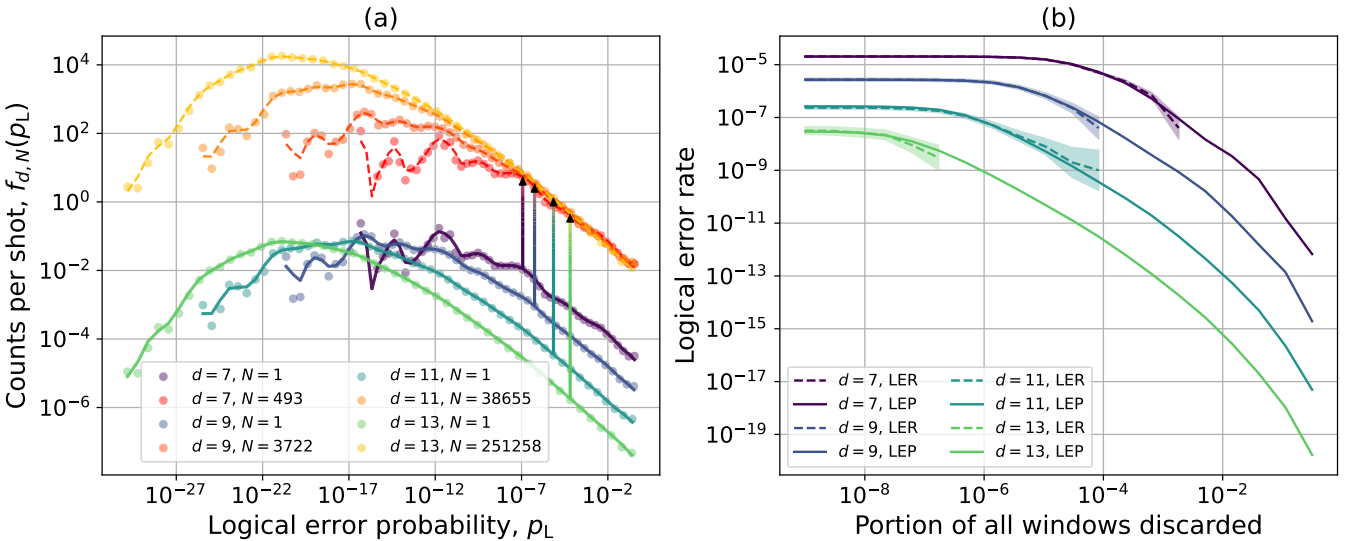


FIG. 6. **Equivalence of different code distances.** (a) Histogram of the calibrated LEPs, normalised by the number of shots, for various numbers of decoding windows in the circuit. The LEPs are grouped in 50 bins of equal logarithmic width. At fixed code distance d , for circuits comprising N windows, we define $f_{d,N}(p_L)$ as the average number of constituent windows whose LEP lies in the bin centred on p_L . The case $N = 1$ (viridis colourmap) corresponds to the normalized LEP histogram for single-window memory experiments. When more windows are added (magma colourmap), all bins gain population at the same rate: $f_{d,N}(p_L) = N f_{d,1}(p_L)$. It is possible to adjust N such that circuits defined by different (N, d) pairs have the same mean P_L ; in this case, the seemingly linear segments of the scaled histograms overlap, as indicated by the upward arrows. (b) The calculated mean LEP (solid) and observed LER (dashed) in a cohort of single-window decoding instances when a fraction of highest- p_L shots are discarded. The curves for $d \in \{11, 13\}$ were obtained with 10^9 shots.

ment comprising many windows.

B. Many-Decoding-Window Statistics

To simplify analysis, we assume (p_L, x) for each window is independent; this simplification is discussed in Section VII. In this case, the total LEP P_L for an experiment comprising N decoding windows, each with LEP $p_{L,i}$, is the probability an odd number of them were wrongly decoded:

$$P_L = \frac{1}{2} \left[1 - \prod_{i=1}^N (1 - 2p_{L,i}) \right]. \quad (3)$$

A valid concern regarding the usefulness of DCSs for error mitigation is scalability: does the distribution of the random variable P_L remain usefully rich in information as the size of the computation increases? One might imagine that, for large enough computations, P_L converges to a sharp value, so that every run with a given code distance and (very large) number of decoding windows N will be found to have a total LEP P_L of, for example, almost exactly 5%. In that case, the useful information gained by evaluating P_L for a given circuit is negligible – it is a foregone conclusion.

In fact, that is not the case. In Section B we analyse the distribution of P_L and find that its variance remains broad (and grows) as N increases, if the code distance

is adjusted to target a fixed LER. However, it could still be the case that, while the variance grows with N , the effective range of LEPs spans fewer orders of magnitude.

To investigate this, we generalise Fig. 5a to circuits of $N \geq 1$ decoding windows and plot the result in Fig. 6a, where the x -axis has additionally been converted to a LEP via the calibration curve. Each single-window LEP histogram is scaled by a factor N such that the mean LEP of an N -window circuit equals 10^{-2} . The evident overlap of the scaled histograms for $p_L > 10^{-7}$ means that the same number of high- p_L windows will be detected for different (N, d) pairs. These rare, high-risk events are precisely the ones which make the dominant contribution to the overall N -window circuit LEP P_L .

Remark 1. Because the non-overlapping parts of the scaled histograms do not contribute much to the overall LEP, the P_L distribution for a numerically intractably large pair (N, d) can be accurately inferred from the P_L distribution for a smaller, testable pair (N', d') yielding the same mean LEP.

The fact that the low- p_L windows bring little contribution to P_L can be seen from Fig. 6b, where we consider the scenario of discarding a fraction of the single-window shots with the highest p_L values. The figure shows both the calculated LEP and the empirically observed LER; these lines agree well. For $d = 13$ it is possible to improve the LER by one (five) orders of magnitude by discarding a fraction 10^{-7} (10^{-3}) of the total shots.

V. DECODER CONFIDENCE SCORES INFORM LOW-OVERHEAD ERROR MITIGATION

In this section, we look at potential applications of the DCS in QEM for logical circuits in the early fault-tolerant era. In Section V A, we present an abort protocol which halts the execution of a deep quantum circuit based on the *instantaneous* DCS. Section V B explains an MLE procedure based on the *whole-circuit* LEP. In Section V C, we combine both methods, applying MLE on increasingly filtered results of an expectation value estimation task. The profound enhancements which we observe represent one of the key aspects of this work. We conclude with an approximate analytical model for a distance-19 surface code, finding that its behaviour closely matches our earlier empirical analyses.

A. Abort Protocol

Suppose we choose the following protocol for executing a logical circuit: abort execution if the DCS associated with *any* decoding window is in a pre-defined ‘discard’ range. Figure 6b immediately leads us to the performance of this approach. Let ρ be the probability a given window is discarded, and p_{kept} be the mean LEP of the retained windows. These quantities correspond respectively to the x and y axes of Fig. 6b. If a circuit of N windows successfully completes, then the expected whole-circuit LEP is approximately $P_{\text{kept}} = \frac{1}{2}[1 - (1 - 2p_{\text{kept}})^N] \approx Np_{\text{kept}}$. As noted, this can be many orders of magnitude lower than when everything is retained. The caveat is that the probability of successfully completing falls as $(1 - \rho)^N$, meaning ρ must be very low for very large circuits. However, there are scenarios in quantum computing where small subroutines can be performed ‘offline’ e.g. when preparing resource states such as magic states or logical Bell pairs [29]. In these cases, an aggressive repeat-until-success model is viable. [5, 15]. The less impressive improvement by one order of magnitude, achieved at much smaller abort rates, can also be used in some early fault-tolerant applications to reduce resource requirements.

B. DCS-Based Maximum Likelihood Estimation

In this subsection, we explain how MLE can be leveraged in expectation value estimation to improve accuracy. We call this technique DCS-MLE.

We consider estimating the expectation value of an observable from M noisy runs of the same quantum circuit comprising N decoding windows. Each run $j \in \{1, \dots, M\}$ has an observed noisy outcome $z_j \in \{-1, +1\}$ and a total LEP $P_{L,j}$ calculated from ϕ . Section C 2 details how we emulate these runs. A straightforward estimator is the unweighted average: $\langle Z_{\text{unmitigated}} \rangle =$

$\frac{1}{M} \sum_{j=1}^M z_j$. However, this can be improved using the data $\{P_{L,j}\}_j$ as follows.

Let us associate a random variable Z_j to each circuit run. The likelihood to observe the set of outcomes $\{z_j\}_{j=1}^M$ is

$$\mathcal{L} = \prod_{j=1}^M \text{pr}(Z_j = z_j), \quad (4)$$

where $\text{pr}(\text{logical statement})$ is the probability the logical statement is true. Let the underlying noiseless outcomes from the logical circuit be $\{\tilde{z}_j\}_{j=1}^M$, all having the same mean, $\langle Z \rangle_{\text{th}}$, such that $\theta := \text{pr}(\tilde{Z}_j = +1) = \frac{1}{2}(1 + \langle Z \rangle_{\text{th}})$. We can express the probability to observe a particular outcome in terms of conditional probabilities on the noiseless outcomes:

$$\text{pr}(Z_j = z_j) = \sum_{\tilde{z}_j} \text{pr}(Z_j = z_j | \tilde{Z}_j = \tilde{z}_j) \text{pr}(\tilde{Z}_j = \tilde{z}_j). \quad (5)$$

Generally, noise corrupts the true outcomes in a non-trivial way, defined by a corruption function q which depends on the logical error probability: $q(P_{L,j}, \tilde{z}_j) := \text{pr}(Z_j = +1 | \tilde{Z}_j = \tilde{z}_j)$. Therefore:

$$\text{pr}(Z_j = +1) = \theta q(P_{L,j}, +1) + (1 - \theta)q(P_{L,j}, -1). \quad (6)$$

Finally, noting that $\text{pr}(Z_j = -1) = 1 - \text{pr}(Z_j = +1)$, the likelihood \mathcal{L} can be written as a function of θ , with the dataset $\{(z_j, P_{L,j})\}_j$ as known parameters. We obtain an estimator for θ by maximising \mathcal{L} , which in practice is done by minimising the negative log-likelihood, $-\ln \mathcal{L}$.

To tackle imperfect $P_{L-\phi}$ calibration, we use a two-parameter fit: we replace $P_{L,j}$ by $\eta P_{L,j}$ in Eq. (6) and also optimise the parameter η . This accounts for an overall rescaling of the original LEP distribution, to ensure the mean LEP matches the true LER.

The function q will depend on the noise propagation in the particular circuit under consideration. For the simple case of a memory experiment, it can be modelled as $q(P_{L,j}, +1) = 1 - P_{L,j}$ and $q(P_{L,j}, -1) = P_{L,j}$.

C. Numerics

We next evaluate the methods from the previous two subsections on emulated results of an expectation value estimation task using a distance-11 surface code (Section V C 1). Three main observations emerge: 1) both methods significantly lower the total error; 2) MLE gives the highest relative improvement over pure abort when applied to unfiltered data; 3) both methods give higher relative improvements as the number of shots increases. We also construct an approximate model for the imperfect mapping between ϕ and λ for a distance-19 surface code and assess the performance of the abort protocol under this model (Section V C 2).

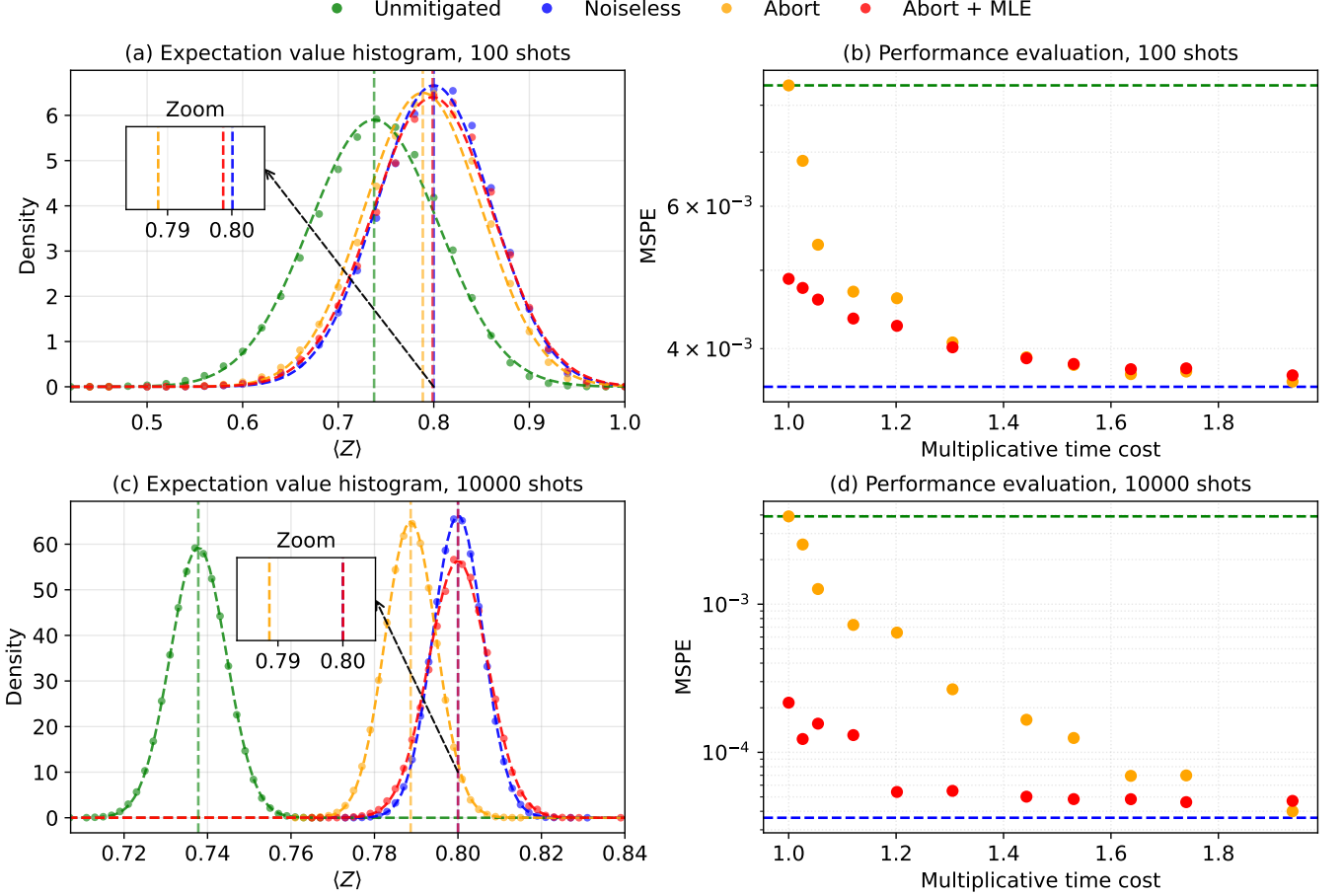


FIG. 7. **Estimating $\langle Z \rangle_{\text{th}} = 0.8$ using a distance-11 surface code, starting from a 7.7(2)% LER in absence of error mitigation.** (a,c) Output distributions of four expectation value estimators, obtained from $N_{\text{rep}} = 2 \times 10^5$ repetitions. Dashed curves are normal distributions with the same mean and variance as their respective datasets, which are shown as dots. The noiseless estimator corresponds to a noiseless quantum computer whose outcome variation is caused solely by statistical Bernoulli fluctuations. The circuit discard fraction is 50%. (b,d) The performance of the four estimators plotted against resource overhead. MSPE is the mean squared prediction error, defined in Eq. (7). The multiplicative time cost calculation is explained in Section D.

1. Distance-11 Surface Code

We set to estimate $\langle Z \rangle_{\text{th}} = 0.8$ from $M_0 \in \{10^2, 10^4\}$ accepted shots with a $d = 11$ surface code, in a circuit comprising $N \approx 2.38 \times 10^5$ decoding windows. We consider a range of abort rates, each of which gives rise to a different LEP distribution for the N -window circuit. Section C describes how we generate the datasets, and Section D explains how we calculate the multiplicative time cost given the abort rate.

In Fig. 7a,c, we show the distribution of outputs from four different estimators. Figure 7b,d shows how they perform as the resource overhead varies. We choose the mean squared prediction error (MSPE):

$$\text{MSPE} := \frac{1}{N_{\text{rep}}} \sum_{i=1}^{N_{\text{rep}}} |\langle Z \rangle_i - \langle Z \rangle_{\text{th}}|^2 \quad (7)$$

as a performance metric as it penalises both bias and variance in the estimated expectation values. Other metrics could be selected based on the task at hand, such as the absolute mean bias (explored in Section G) or the probability to obtain an estimate within a desired range.

There are several effects to be noted. First, aborting a greater portion of risky circuit executions steadily improves performance. Second, MLE reduces errors even without discarding any circuit executions. Its relative advantage diminishes as the abort protocol becomes more aggressive. It is noteworthy that near-noiseless performance can be achieved with MLE on carefully filtered results. Finally, the benefit of using MLE increases with the number of accepted shots, because it becomes easier to extract signal.

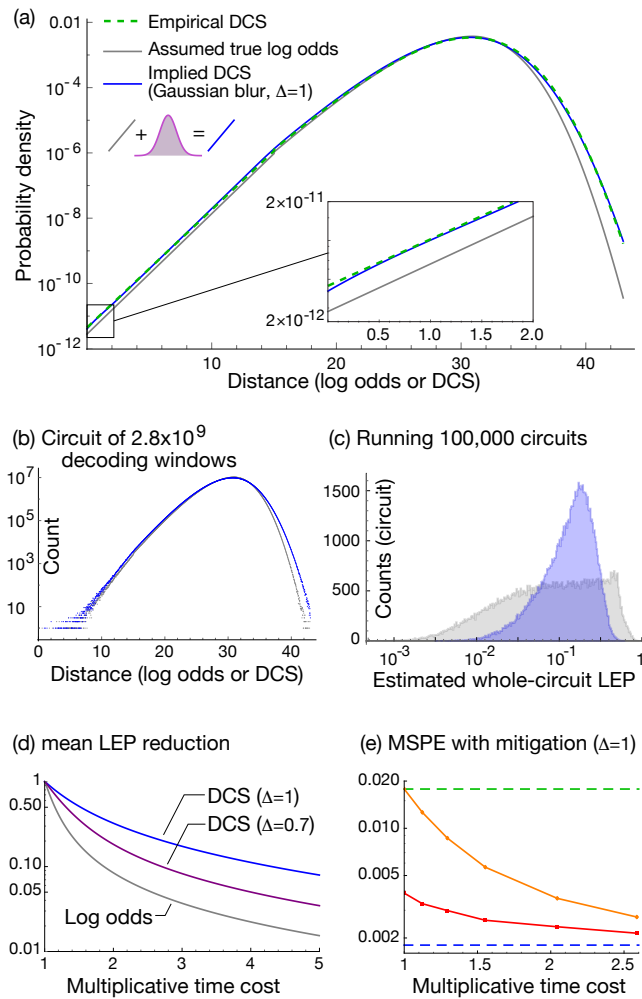


FIG. 8. Contrasting the at-scale performance of the DCS (blue) versus the ideal but impractical-to-compute log odds λ (gray). In all cases the chosen DCS is the swim distance. In panel (a) the green dashed line shows the fitted probability density function of *measured* DCS values for decoding windows of a distance-19 surface code, by binning the calibration data into 500 bins. An assumed probability curve for λ is shown in gray, and in blue an *implied* DCS distribution derived by redistributing λ via a Gaussian with standard deviation $\Delta = 1$. We see a good match between green and blue. Using the distributions in (a) we generate sets of 2.8×10^9 scores, representing all decoding windows in a large circuit; an example distribution is shown in (b). From such a set we infer the probability P_L of error in the circuit; repeating this 10^5 times we obtain distribution (c) with mean $P_L = 0.153$. We note that relying on the DCS means we cannot identify very high or very low risk circuits, as we would with access to λ . Panel (d) shows the factor by which we reduce error rates using abort criteria, at the cost of increased quantum processor time. Panel (e) is the equivalent of Fig. 7b,d with the same meaning for lines, but with an intermediate number of shots: 200.

2. Distance-19 Surface Code

We cannot perform the same simulation for $d = 19$ as no logical errors were observed during calibration, but we can estimate its performance with the following model. In the absence of a known distribution of the log success odds λ , we use the distribution of measured DCS values for $d = 19$ and slightly deform it, until the mean p_L associated with this deformed distribution matches the one predicted from our statistics (see Fig. B.1a). We then use Eq. (2) and assume r follows a Gaussian distribution with mean zero and variance $\Delta = 1$. The inferred distribution of DCS values closely matches that of the measured ones, as seen in Fig. 8a. This is therefore an entirely analytic model, in which we have descriptions of λ and the DCS. Moreover, we know the range of λ associated with each DCS value, so there is no need to calibrate the DCS – in a real scenario, imperfect calibration would indeed be a factor in performance; further work could explore the impact of this.

Figure 8d shows impressive improvement in the whole-circuit LEP when we impose an abort condition based on the instantaneous window DCS. As suggested by the observation in Section IV B that most of the logical error risk is contained in a few very risky windows, we see the post-selection method does not require exponential overhead for a linear decrease in LER (for a significant range of reduction). However, we do observe that DCS accuracy is very significant in the amount of reduction. Recall that Section III established a close match between the swim distance and λ ; even so, we see in Fig. 8c,d that the imperfect correlation manifests in a considerable worsening of the quality of the information we obtain about the whole-circuit LEP. Note that the $\Delta = 1$ assumption is somewhat pessimistic as an extrapolation from Fig. 4, and with a modest reduction to $\Delta = 0.7$ the performance dramatically improves. Conversely, if we were to replace the swim distance with an alternative DCS that is significantly weaker, it is possible that the whole-circuit LEP mitigations explored in this paper would become ineffective.

Finally in Fig. 8e we generate the equivalent of the earlier panels in Fig. 7b,d. It is reassuring that the key qualitative features are again seen in this alternative model.

VI. APPLICATIONS

We now discuss applications of the abort protocol and DCS-MLE in quantum phase estimation (QPE) algorithms. In Section VI A, we perform a detailed resource estimate of our protocols for a Hubbard model ground state energy estimation problem, using statistical QPE. In Section VI B, we qualitatively describe possible uses of DCS-MLE in other applications.

A. Hubbard Model Resource Estimation

In this subsection, we apply our findings to reduce the resource requirements for the implementation of a full logical circuit. Specifically, we find that the surface code distance can be reduced from 21 to 19 and achieve the same LER with a 64% time overhead via the abort protocol. This is a conservative estimate; depending on the metric used to assess logical performance, it could be achieved by MLE without any additional overhead.

We target estimating the ground state energy of the 10×10 Hubbard model to 10^{-2} statistical accuracy (in absence of physical noise) and at most 10^{-2} LER (from noise added on top of statistical fluctuations), following the QCELS-based [30] resource estimates in Ref. [31]. The algorithm involves executing $N_{\text{circuits}} = 160$ different quantum circuits of various depths, each repeated with $M_0 = 100$ shots to estimate an observable's expectation value. This means that $N_{\text{executions}} = N_{\text{circuits}} M_0$ circuit executions would take place in practice. Section E provides more algorithmic details. We estimate that an implementation that does not use the DCS requires a $d_{\text{targ}} = 21$ surface code, which corresponds to a LER of approximately $R_{\text{targ}} = 8.4 \times 10^{-3}$; this is our target LER.

The potential advantage of the DCS arises during the estimation of expectation values. We explore whether the necessary quantum circuits can be executed with a smaller $d_{\text{small}} = 19$ code (at an unmitigated LER of $R_{\text{small}} = 7.7(4)\%$) and still meet the target LER via QEM. Therefore, the desired improvement in the LER is $R_{\text{small}}/R_{\text{targ}} = 10.91$. We emulate the behaviour of the $d = d_{\text{small}}$ code using $d = 11$ and Remark 1. In Section VC1, the number of decoding windows was chosen precisely to approximate the LEP distributions for $d = d_{\text{small}}$.

By repeatedly sampling $N_{\text{executions}}$ times from the emulated experiment distribution used in Section VC1 at a 60% discard fraction, we estimate that the 95% confidence interval for the effective LER is $[0.59\%, R_{\text{targ}}]$, thus achieving the target LER or better, at a 21% increase in spacetime volume (calculated in Section F).

For this algorithm, it may be more useful to analyse the MSPE instead of the effective LER. Using the data shown in Fig. 7, we find that the target MSPE (0.376×10^{-2}) is achieved by the pure-abort strategy with a similar discard fraction as reported above: 60%. MLE does not give a significant improvement in these cases due to the large Bernoulli variance of 100 shots. However, in contexts where the bias is more important than the variance, MLE could achieve the target without any time overhead, as discussed in Section G.

To summarise, we explore the Hubbard model application in a scaled-down form which allows us to apply our earlier empirical results from Section VC1. We believe that for the full problem it should be possible to reduce the surface code distance from 21 to 19 at a marginal increase in space-time volume. The advantage here is that the application could run successfully on a smaller quantum computer.

B. Other Applications

In ancilla-based QPE [32], the final outcome of the noiseless circuit is a bitstring of length n that estimates the first n bits of a desired phase. The noiseless circuit can be run multiple times, resulting in a histogram of output bitstrings; these outputs will get scrambled in the presence of noise. Ref. [33] describes an MLE protocol (based on quasiprobability methods) suitable for deducing the target bitstring. We believe this protocol could be improved using the DCS.

As suggested in Section VC1, DCS-MLE would be very useful in algorithms that do not take full advantage of Heisenberg scaling and instead exploit a trade-off between the number of different circuits run and the number of times each one is repeated [34–37].

VII. DISCUSSION AND OUTLOOK

This paper brings more nuance to the existing works on decoder confidence and provides a proof of principle for error mitigation. We identify four limitations/further directions of research.

Firstly, the tensor network method we used to compute λ was prone to numerical imprecision as there were many samples that led to division by zero or negative odds. For the remaining samples, floating-point precision capped the λ values at 16, meaning we were analysing a very restricted subset of cases, especially at large code distances where it is known that λ can far exceed 16.

Secondly, to maintain decoding accuracy, most decoding schemes [21, 38–40] require neighbouring decoding windows in a quantum computation to overlap: for a code of distance d , the overlap is usually of the order $d/2$ [41]. This means decoding windows are not independent; accounting for this effect would alter Eq. (3). Moreover, numerical results for N -window circuits made use of emulated logical errors, obtained under the assumption of window independence, so they should be trusted with caution.

Thirdly, regarding DCS-based QEM, the calibration curves for large code distances take a long time to obtain because the LEPs are so low. Thus, full calibration curves would have to be provided by the quantum device manufacturers. Nevertheless, Fig. 5b shows that the calibration curves are extremely similar for the same noise model between different code distances, so an approximate calibration curve for $d = 19$ could be derived from lower distances.

Lastly, we emulated deep logical circuits by stitching together the results from individual memory experiments. A more comprehensive simulation would account for multiple interacting logical qubits, meaning the corruption function q would in general be nonlinear in $P_{L,j}$.

Note that a single-logical-qubit Pauli noise model can be constructed for general circuits based on the DCS. We can consider a computational model with layers of logical operations, between which d cycles of stabiliser measurements are performed on each logical qubit. Hence, each logical qubit experiences an X , Y , or Z error with a probability given by the DCS.

A fundamental question concerning our proposed methods is whether the abort protocol is scalable to large code distances (beyond the early FT era). Most existing works have focused on applications of the DCS with small (< 11) distances due to scalability: the sampling overhead of the abort protocol could be unreasonably high. Section IV provides numerical evidence against this idea by considering the statistical properties of the DCS distribution and demonstrating that the method works for a small code with the same LER as a larger one. Ref. [15] provides alternative evidence towards scalability: the authors find numerically that the rate at which the decoder aborts a circuit run exhibits threshold behaviour. Namely, for a fixed abort tolerance, if the physical error rate is below (above) some threshold, the abort rate decreases (increases) as the code distance increases. They observe that the threshold is on the order of 10^{-2} for the code capacity noise model, and expect it to decrease under more realistic noise models. Nevertheless, as long as the abort threshold does not drop below 10^{-4} , post-selection remains a valuable tool for useful applications in the early fault-tolerant era, such as the QPE routine described in Section VIB.

VIII. CONCLUSION

We have shown that the log success odds of a decoding instance can be very well approximated by both the complementary gap and the swim distance for MWPM under phenomenological noise, justifying their status as DCSs. For a simplified model of window-based decoding under circuit-level noise, we have shown that DCSs remain rich in information as the circuit size increases, which suggests that they can be used for more complex tasks than state preparation. Finally, we have explored this latter idea in the form of QEM techniques for the early fault-tolerant quantum computing era, where aborting and MLE can help run useful applications with a quantum device of limited size. We emphasise that our results rely on the observation that the swim distance is an excellent DCS; the performance of both proposed QEM methods diminishes as the DCS quality decreases. This motivates future work toward even more accurate DCS methods.

ACKNOWLEDGMENTS

We thank Zi-Han Chen for providing code and guidance on their implementation of the swim distance on MWPM. We also thank Christophe Piveteau for providing

code for calculating logical coset probabilities via tensor network contraction. For useful discussions, we thank Zhenyu Cai, Armands Strikis and Christopher Chubb. We acknowledge the use of the University of Oxford Advanced Research Computing (ARC) facility [42] in carrying out this work and specifically the facilities made available from the EPSRC QCS Hub grant (agreement No. EP/T001062/1). We also acknowledge support from two EPSRC projects: RoaRQ (EP/W032635/1) and SEEQA (EP/Y004655/1). TC and MD acknowledge support from EPSRC DTP studentships. TC was supported by JST ASPIRE Japan Grant Number JPMJAP2319.

AUTHOR CONTRIBUTIONS

TC conceived and performed the tensor network comparison in Section III. MD designed the DCS-MLE procedure and performed the analyses in Sections IV and VC1, and the resource estimation in Section VIA. SCB performed the analysis in Section VC2 and supervised the project. All authors contributed equally to writing the manuscript.

Note added: In the final days of preparation of this manuscript, a related preprint [43] was announced with similar ideas on using the DCS for error mitigation. For example, the authors consider using the DCS for entire logical circuits and reach similar conclusions using the same abort-based method; they also assess the accuracy of the complementary gap using a tensor network decoder. While similar, there are differences. The authors use a code capacity noise model and emulate logical gates; we adopt a more realistic circuit-level noise model but emulate only quantum memory experiments. The authors propose a ZNE procedure based on probabilistic error amplification, whereas the MLE procedure we propose is based on the LEP variation between runs.

Shortly after the first version of this manuscript was announced, another related preprint [44] was announced that proposes a logical error mitigation protocol called SALEM, conditioned directly on the decoder syndrome. The authors treat different syndromes as inducing different logical error channels, and syndrome-dependent mitigation or rejection strategies are applied to reduce logical errors at the channel level. While both our work and theirs exploit run-to-run variability in LEP and abort risky circuit executions based on the DCS, they differ substantially in methodology. For accepted executions, SALEM mitigates errors via inverting logical error channels, whereas our approach further uses the DCS as a parameter in classical post-processing via maximum-likelihood estimation. The requirements to implement the methods are also different: SALEM requires channel characterisation, while DCS-MLE requires a calibrated mapping between the window-level DCS and the LEP.

[1] P. W. Shor, Scheme for reducing decoherence in quantum computer memory, *Physical Review A* **52**, R2493 (1995), publisher: American Physical Society.

[2] A. G. Fowler, M. Mariantoni, J. M. Martinis, and A. N. Cleland, Surface codes: Towards practical large-scale quantum computation, *Physical Review A* **86**, 032324 (2012), publisher: American Physical Society.

[3] Z.-H. Chen, M.-C. Chen, C.-Y. Lu, and J.-W. Pan, Efficient magic state cultivation on \mathbb{RP}^2 (2025), arXiv:2503.18657 [quant-ph].

[4] N. Meister, C. A. Pattison, and J. Preskill, Efficient soft-output decoders for the surface code (2024), arXiv:2405.07433 [quant-ph].

[5] S.-H. Lee, L. English, and S. D. Bartlett, Efficient post-selection for general quantum LDPC codes (2025), arXiv:2510.05795 [quant-ph].

[6] H. Bombín, M. Pant, S. Roberts, and K. I. Seetharam, Fault-Tolerant Postselection for Low-Overhead Magic State Preparation, *PRX Quantum* **5**, 010302 (2024), publisher: American Physical Society.

[7] A. deMarti iOlius, P. Fuentes, R. Orús, P. M. Crespo, and J. Etxezarreta Martinez, Decoding algorithms for surface codes, *Quantum* **8**, 1498 (2024).

[8] C. Gidney, M. Newman, P. Brooks, and C. Jones, Yoked surface codes, *Nature Communications* **16**, 4498 (2025).

[9] C. A. Pattison, A. Krishna, and J. Preskill, Hierarchical memories: Simulating quantum LDPC codes with local gates, *Quantum* **9**, 1728 (2025).

[10] Y. Akahoshi, R. Toshio, J. Fujisaki, H. Oshima, S. Sato, and K. Fujii, Runtime reduction in lattice surgery utilizing time-like soft information (2025), arXiv:2510.21149 [quant-ph].

[11] S. Sunami, Y. Hirano, T. Hinokuma, and H. Yamasaki, Entanglement boosting: Low-volume logical Bell pair preparation for distributed fault-tolerant quantum computation (2025), arXiv:2511.10729 [quant-ph].

[12] D. Poulin, Optimal and efficient decoding of concatenated quantum block codes, *Physical Review A* **74**, 052333 (2006).

[13] H. Goto and H. Uchikawa, Fault-tolerant quantum computation with a soft-decision decoder for error correction and detection by teleportation, *Scientific Reports* **3**, 2044 (2013).

[14] A. Siegel, Z. Cai, H. Jnane, B. Koczor, S. Pexton, A. Strikis, and S. Benjamin, Snakes on a Plane: mobile, low dimensional logical qubits on a 2D surface (2025), arXiv:2501.02120 [quant-ph].

[15] S. C. Smith, B. J. Brown, and S. D. Bartlett, Mitigating errors in logical qubits, *Communications Physics* **7**, 386 (2024).

[16] P. Sales Rodriguez, J. M. Robinson, P. N. Jepsen, Z. He, C. Duckering, C. Zhao, K.-H. Wu, J. Campo, K. Bagnall, M. Kwon, T. Karolyshyn, P. Weinberg, M. Cain, S. J. Evered, A. A. Geim, M. Kalinowski, S. H. Li, T. Manovitz, J. Amato-Grill, J. I. Basham, L. Bernstein, B. Braverman, A. Bylinskii, A. Choukri, R. J. DeAngelo, F. Fang, C. Fieweger, P. Frederick, D. Haines, M. Hamdan, J. Hammett, N. Hsu, M.-G. Hu, F. Huber, N. Jia, D. Kedar, M. Kornjača, F. Liu, J. Long, J. Lopatin, P. L. S. Lopes, X.-Z. Luo, T. Macrì, O. Marković, L. A. Martínez-Martínez, X. Meng, S. Ostermann, E. Ostroumov, D. Paquette, Z. Qiang, V. Shofman, A. Singh, M. Singh, N. Sinha, H. Thoreen, N. Wan, Y. Wang, D. Waxman-Lenz, T. Wong, J. Wurtz, A. Zhdanov, L. Zheng, M. Greiner, A. Keesling, N. Gemelke, V. Vuletić, T. Kitagawa, S.-T. Wang, D. Bluvstein, M. D. Lukin, A. Lukin, H. Zhou, and S. H. Cantú, Experimental demonstration of logical magic state distillation, *Nature* **645**, 620 (2025).

[17] C. Gidney, N. Shutty, and C. Jones, Magic state cultivation: growing T states as cheap as CNOT gates (2024), arXiv:2409.17595 [quant-ph].

[18] K. Sahay, P.-K. Tsai, K. Chang, Q. Su, T. B. Smith, S. Singh, and S. Puri, Fold-transversal surface code cultivation (2025), arXiv:2509.05212 [quant-ph].

[19] N. Shutty, M. Newman, and B. Villalonga, Efficient near-optimal decoding of the surface code through ensembling (2024), arXiv:2401.12434 [quant-ph].

[20] R. Toshio, K. Kishi, J. Fujisaki, H. Oshima, S. Sato, and K. Fujii, Decoder switching: Breaking the speed-accuracy tradeoff in real-time quantum error correction (2025), arXiv:2510.25222 [quant-ph].

[21] E. Dennis, A. Kitaev, A. Landahl, and J. Preskill, Topological quantum memory, *Journal of Mathematical Physics* **43**, 4452 (2002).

[22] A. Hutter, J. R. Wootton, and D. Loss, Efficient Markov chain Monte Carlo algorithm for the surface code, *Physical Review A* **89**, 022326 (2014).

[23] C. Piveteau, C. T. Chubb, and J. M. Renes, Tensor-Network Decoding Beyond 2D, *PRX Quantum* **5**, 040303 (2024), publisher: American Physical Society.

[24] H. Chen, D. Xu, G. M. Sommers, D. A. Huse, J. D. Thompson, and S. Gopalakrishnan, Scalable accuracy gains from postselection in quantum error correcting codes (2025), arXiv:2510.05222 [cond-mat.stat-mech].

[25] D. Bluvstein, S. J. Evered, A. A. Geim, S. H. Li, H. Zhou, T. Manovitz, S. Ebadi, M. Cain, M. Kalinowski, D. Hangleiter, J. P. Bonilla Ataides, N. Maskara, I. Cong, X. Gao, P. Sales Rodriguez, T. Karolyshyn, G. Semeghini, M. J. Gullans, M. Greiner, V. Vuletić, and M. D. Lukin, Logical quantum processor based on reconfigurable atom arrays, *Nature* **626**, 58 (2024).

[26] L. H. English, D. J. Williamson, and S. D. Bartlett, Thresholds for postselected quantum error correction from statistical mechanics, *Physical Review Letters* **135**, 120603 (2025).

[27] O. Higgott and C. Gidney, Sparse Blossom: correcting a million errors per core second with minimum-weight matching, *Quantum* **9**, 1600 (2025).

[28] C. Gidney, Stim: a fast stabilizer circuit simulator, *Quantum* **5**, 497 (2021).

[29] E. Knill, Quantum computing with realistically noisy devices, *Nature* **434**, 39 (2005).

[30] Z. Ding and L. Lin, Even Shorter Quantum Circuit for Phase Estimation on Early Fault-Tolerant Quantum Computers with Applications to Ground-State Energy Estimation, *PRX Quantum* **4**, 020331 (2023), publisher: American Physical Society.

[31] Y. Akahoshi, R. Toshio, J. Fujisaki, H. Oshima, S. Sato, and K. Fujii, Compilation of Trotter-Based Time Evolution for Partially Fault-Tolerant Quantum Computing Architecture (2024), arXiv:2408.14929 [quant-ph].

- [32] M. A. Nielsen and I. L. Chuang, *Quantum computation and quantum information*, 10th ed. (Cambridge university press, Cambridge, 2010).
- [33] A. Dutkiewicz, S. Polla, M. Scheurer, C. Gogolin, W. J. Huggins, and T. E. O’Brien, **Error mitigation and circuit division for early fault-tolerant quantum phase estimation** (2024), arXiv:2410.05369 [quant-ph].
- [34] H. Ni, H. Li, and L. Ying, **On low-depth algorithms for quantum phase estimation**, *Quantum* **7**, 1165 (2023), publisher: Verein zur Förderung des Open Access Publizierens in den Quantenwissenschaften.
- [35] D. Wang, O. Higgott, and S. Brierley, **Accelerated Variational Quantum Eigensolver**, *Physical Review Letters* **122**, 140504 (2019), publisher: American Physical Society.
- [36] Z. Ding and L. Lin, **Simultaneous estimation of multiple eigenvalues with short-depth quantum circuit on early fault-tolerant quantum computers**, *Quantum* **7**, 1136 (2023), arXiv:2303.05714 [quant-ph].
- [37] J. S. Nelson and A. D. Baczewski, **Assessment of quantum phase estimation protocols for early fault-tolerant quantum computers**, *Physical Review A* **110**, 042420 (2024), publisher: American Physical Society.
- [38] L. Skoric, D. E. Browne, K. M. Barnes, N. I. Gillepie, and E. T. Campbell, **Parallel window decoding enables scalable fault tolerant quantum computation**, *Nature Communications* **14**, 7040 (2023).
- [39] H. Bombín, C. Dawson, Y.-H. Liu, N. Nickerson, F. Pastawski, and S. Roberts, **Modular decoding: parallelizable real-time decoding for quantum computers** (2023), arXiv:2303.04846 [quant-ph].
- [40] T. Chan, **Snowflake: A distributed streaming decoder** (2024), arXiv:2406.01701 [quant-ph].
- [41] S. Fuhui Lin, E. C. Peterson, K. Sankar, and P. Sivarajah, **Spatially parallel decoding for multi-qubit lattice surgery**, *Quantum Science and Technology* **10**, 035007 (2025).
- [42] A. Richards, *University of Oxford Advanced Research Computing* (2015).
- [43] Z. Zhou, S. Pexton, A. Kubica, and Y. Ding, **Error mitigation of fault-tolerant quantum circuits with soft information** (2025), arXiv:2512.09863 [quant-ph].
- [44] D. Aharonov, Y. Atia, E. Bairey, Z. Brakerski, I. Cohen, O. Golan, I. Gurwich, N. H. Lindner, and M. Shitman, **Syndrome aware mitigation of logical errors** (2025), arXiv:2512.23810 [quant-ph].

Appendix A: Calculating the Sources of Variation of the DCS

First, we describe how we obtained σ_r . We emulated the unrotated surface code under a perturbed phenomenological noise model (described in Section A 1). For odd distances 3 to 11, we randomly sampled syndromes obtained from noise levels in 10^{-4} to 10^{-1} . For each syndrome, we calculated both DCS values using the MWPM decoder [27], then calculated λ via tensor-network contraction [23] (details in Section A 2). The results are shown in Fig. A.1 and suggest that α is linear for both DCSs. Therefore, we fit a line $\hat{\phi}(\lambda)$ to the data $\{(\lambda_i, \phi_i)\}_{i=1}^n$ for each distance and estimate σ_r by

calculating the *sample root mean squared residual*:

$$\widehat{\sigma_r} = s_r := \sqrt{\frac{\sum_{i=1}^n [\phi_i - \hat{\phi}(\lambda_i)]^2}{n-1}}. \quad (\text{A1})$$

To obtain $\sigma_{\alpha(\lambda)}$, we calculated both DCS values for 10^8 randomly sampled syndromes at a fixed noise level of 10^{-3} , then calculated the sample variance s_ϕ^2 for each DCS. Finally, we note that Eq. (2) and the independence of λ and r implies $\sigma_\phi^2 = \sigma_{\alpha(\lambda)}^2 + \sigma_r^2$, so we estimate $\sigma_{\alpha(\lambda)}$ by calculating

$$\widehat{\sigma_{\alpha(\lambda)}} = \sqrt{s_\phi^2 - s_r^2}, \quad (\text{A2})$$

where s_r is taken from Eq. (A1).

1. Perturbed Phenomenological Noise Model

In the phenomenological noise model, all edges have the same weight, giving rise to a very limited set of possible values the DCS can take. We found that this led to a large value for s_r in Eq. (A1); however, such a simplistic noise model is unrealistic. Ideally, we would perform our analysis in Section III using a circuit-level noise model whose edge weights are calibrated from experiments or existing syndrome data. Although Ref. [23] provides a tensor-network decoder for circuit-level noise, we could not obtain values of λ that converged quickly enough. Therefore, we resorted to a ‘perturbed’ phenomenological noise model, wherein each edge weight is multiplied by a random scalar drawn uniformly from $[1-\delta, 1+\delta]$. We set $\delta = 0.3$ which roughly corresponds to the variation in edge weights for standard circuit-level depolarising noise of strength $p = 10^{-3}$ [28].

2. Tensor Network Contraction

We use the software package `tndecoder3d` introduced in Ref. [23]. For the surface code under phenomenological noise, the network to contract resembles a 3D cubic lattice. The contraction algorithm first contracts the 3D lattice down to a 2D lattice, then contracts the 2D lattice using well-known techniques. Following Ref. [23], we use a maximum bond dimension of 24 and 32 for each stage respectively. Figure A.2 shows that these values, respectively named ‘3D bond dimension’ and ‘2D bond dimension’, are sufficient for s_r in Eq. (A1) to converge.

Appendix B: LEP Variance of a Many-Window Experiment

As discussed in the main text, the total LEP for an experiment comprising N windows, each with LEP $p_{L,i}$

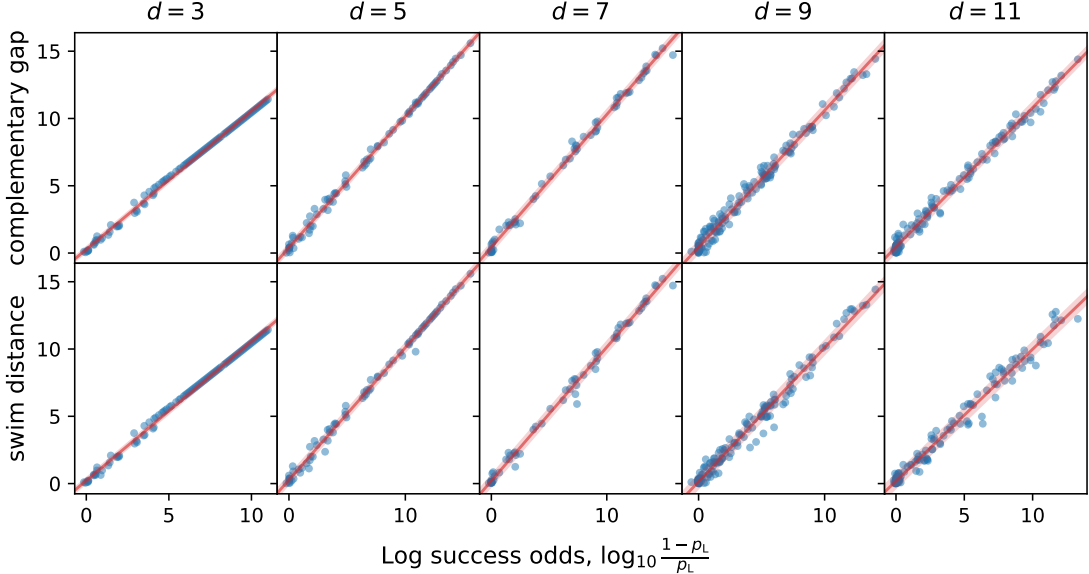


FIG. A.1. Decoder confidence score ϕ plotted against log success odds λ for different code distances d . Each blue point is one syndrome sample from the unrotated surface code under a perturbed phenomenological noise model, decoded using MWPM. The best-fit line calculated using Unweighted Least Squares is shown in red; the height of the shaded region is the root mean squared residual, and is plotted as σ_r in Fig. 4. Due to floating-point precision the λ values are capped at 16, so we ignore samples whose complementary gap exceeds 16.

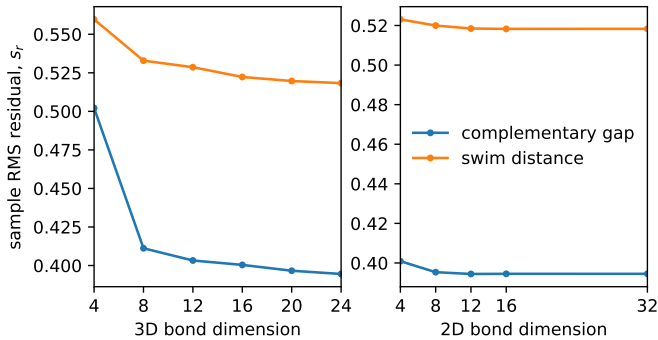


FIG. A.2. The sample root mean squared residual of the log success odds plotted against the bond dimensions used for each stage of tensor network contraction, for the distance-11 surface code.

is given by Eq. (3). If all $p_{L,i}$ have mean $\mu_{1,d}$ and variance $\sigma_{1,d}^2$, the random variable P_L has mean and variance:

$$\mu_{N,d} = \frac{1}{2} [1 - (1 - 2\mu_{1,d})^N], \quad (B1)$$

$$\sigma_{N,d}^2 = \frac{1}{4} \{ [(1 - 2\mu_{1,d})^2 + (2\sigma_{1,d})^2]^N - (1 - 2\mu_{1,d})^{2N} \}. \quad (B2)$$

Figure B.1a shows that both $\mu_{1,d}$ and $\sigma_{1,d}^2$ are very small; in this case, $\sigma_{N,d}^2$ vanishes at constant d as $N \rightarrow \infty$. In practical contexts however, the distribution of P_L remains broad (and thus useful) as circuit sizes increase. The explanation lies in the observation that, as N increases, the mean total LEP $\mu_{N,d}$ also increases at constant d , possibly exceeding the maximum error allowed

for the particular application under consideration; see Fig. B.1b. The solution is to increase the code size: for a fixed target LER ϵ , we choose the smallest code distance $d(\epsilon)$ that fulfils $\mu_{N,d(\epsilon)} \leq \epsilon$. The question then becomes: how does $\sigma_{N,d(\epsilon)}^2$ behave? Figure B.1c indicates that this variance does not shrink as N increases.

Appendix C: Numerical Simulation

1. Abort Protocol

Here, we describe how we generate datasets for the LEP and logical error of each N -window circuit. We perform simulations up to a code distance of 11, which is the largest distance at which enough logical errors could be detected during calibration within 10^8 shots. To avoid simulating deep circuits and calculating their DCS values, we emulate the behaviour of a circuit comprising $N = 2.38 \times 10^5$ windows by sampling from a pool of single-window circuits, each characterised by a calibrated LEP p_i and a logical error $x_i \in \{0, 1\}$, where $x_i = 0$ indicates successful decoding. The N -window circuit is considered to have experienced an error if the decoding of an odd number of the N windows failed: $X = 1$ if $\sum_{i=1}^N x_i$ is odd, else $X = 0$. The assigned LEP for an N -window circuit is given by Eq. (3).

Next, we explain how the abort protocol affects the LEP distribution. Let the single-window abort rate be ρ , achieved by setting some LEP threshold. This means that, in an N -window circuit, each window has an LEP

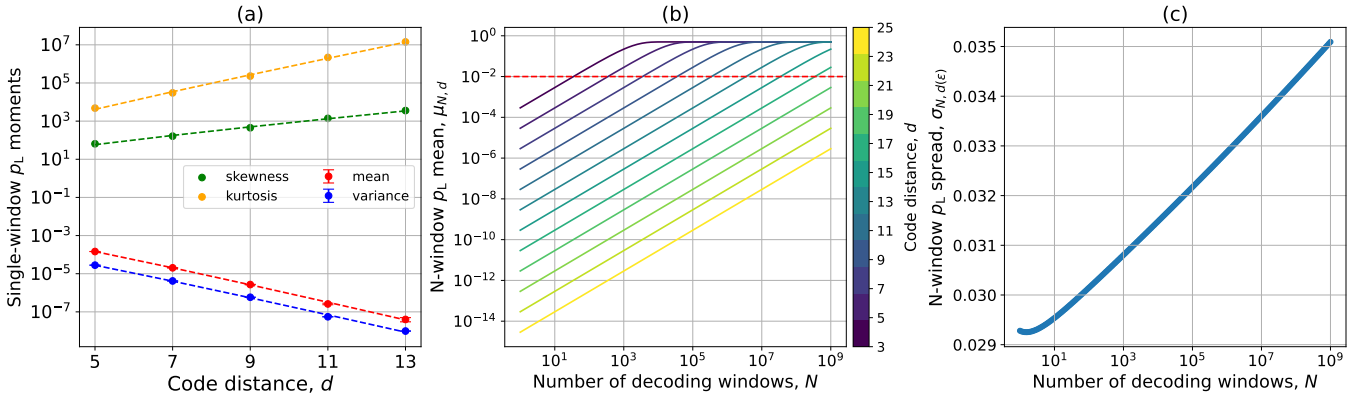


FIG. B.1. **Characteristics of LEP distributions.** (a) The moments of the p_L distributions emerging from the single-window memory experiments have a clean dependence on d , so we can predict the distribution moments for higher code distances. (b) The mean LEP of a full circuit involving N decoding windows, for various choices of code distance d . As N increases with d fixed, eventually we fail to meet any fixed target accuracy such as the 10^{-2} marked here in red. (In Fig. 6 we use values of N corresponding to the intersections of the curves and the red line here.) (c) When choosing the smallest code distance $d(\epsilon)$ for which $\mu_{N,d(\epsilon)} \leq \epsilon = 0.01$, the variance $\sigma_{N,d(\epsilon)}^2$ of the total LEP slowly increases with N .

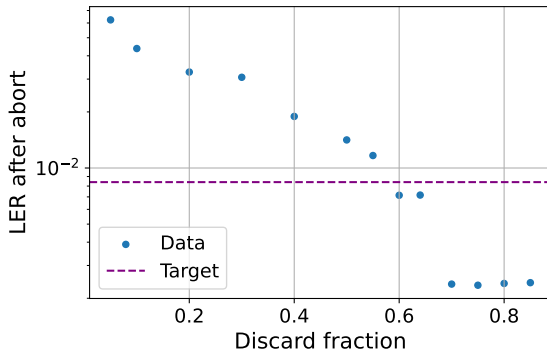


FIG. C.1. Logical error rate of the retained executions for different discard fractions at $d = 11$, obtained by sampling $N = 2.38 \times 10^5$ single-window (x, p_L) pairs 10^6 times. The target LER is specific to the Hubbard model application described in Section VIA.

larger than that threshold with probability ρ . The probability to discard the circuit by aborting at any point throughout its run is $f = 1 - (1 - \rho)^N$. Throughout this work, we refer to f as the discard fraction. This is analogous to Fig. 8d.

To obtain the LEP distribution for a certain abort rate, we eliminate all the single-window experiments from the 10^8 cohort whose LEP is above the threshold LEP. We then proceed as described in the first paragraph of this appendix subsection and sample N windows 10^6 times. In Fig. C.1, we show the retained LER decay with discard fraction.

For the resource estimation task described in Section VIA, we notice that a 60% discard fraction brings the LER down to the target value. Therefore, we sample $M = 16\,000$ times from the $\{(X_j, P_{L,j})\}$ dataset obtained

at the abort rate associated with this discard fraction, effectively emulating M instances of N -window circuits. The empirical LER is the mean X across the M accepted shots, and is stated in the main text with a 95% confidence interval.

2. Expectation Value Estimation

Here, we describe how we generate datasets to emulate M noisy experiments, each being an N -window circuit execution. First, we emulate M copies of a $|\bar{0}\rangle$ memory experiment as described in Section C1 to obtain the LEPs $\{P_{L,j}\}_{j=1}^M$ from the DCS and the logical errors $\{X_j\}_{j=1}^M$. Next, for a fixed ideal expectation value $\langle Z \rangle_{\text{th}}$, we employ a random number generator to generate the noiseless logical outcomes $\{\tilde{Z}_j \in \{-1, +1\}\}_{j=1}^M$, where $\tilde{Z}_j = +1$ occurs with probability $(1 - \langle Z \rangle_{\text{th}})/2$. We then randomise the signs of the noiseless outcomes according to the logical errors $\{X_j\}_{j=1}^M$ to obtain the noisy outcomes $Z_j = \tilde{Z}_j(1 - X_j) - UX_j$, where U is a random variable with equal probability to take value $+1$ or -1 . This setup provides an effective framework for modelling arbitrary logical circuits similar to memory experiments, both when using and not using the abort protocol. Note that we had to make an assumption about how the noise influences the final outcome. For a memory experiment, the outcome would actually be 100% flipped by a logical error, but assuming randomisation instead is more likely for general circuits and algorithms.

Appendix D: Multiplicative Time Cost Caused by Aborting

Here, we calculate the multiplicative time cost required to obtain M_0 accepted shots based on the abort rate. The advantage of aborting is that it saves time by not letting a circuit-to-be-discarded complete. For an N -window circuit which aborts at some point throughout its execution, we want to know, on average, how far the execution proceeds before it is aborted. We define $p_{\text{abort}}(n)$ as the probability that the circuit aborts because of the n^{th} window. This requires that the current window causes the abort, and additionally that none of the previous windows have caused it. Therefore, $p_{\text{abort}}(n) = \rho(1 - \rho)^{n-1}/f$. The average window at which the abort happens (provided that it happens) is calculated as $\langle n \rangle = \sum_{i=1}^N np_{\text{abort}}(n)$. We divide this by N to obtain the average fraction of circuit executed before abort:

$$\frac{\langle n \rangle}{N} = \frac{1 - (1 - f)(1 + N\rho)}{N\rho f}. \quad (\text{D1})$$

Let M_0 be the desired number of shots for the quantum task, and M the number of executed shots when the abort rate is ρ . They are related by $(1 - f)M = M_0$. Of these M executions, a fraction $1 - f$ complete, thus contributing fully to the time duration, while the other fraction f contribute an average of $\frac{\langle n \rangle}{N}$. Overall, the mean multiplicative time cost caused by aborting at rate ρ becomes:

$$\omega := \frac{1 - f + f\langle n \rangle/N}{1 - f} = \frac{f/N}{(1 - f)[1 - (1 - f)^{1/N}]}. \quad (\text{D2})$$

Appendix E: QCELS Parameters

Based on numbers reported in [31] for the chosen algorithmic accuracy (the maximum number of Trotter steps involved in any quantum circuit and the average number of clocks per Trotter step), we deduced that the maximum number of decoding windows in any quantum circuit is 1.38×10^9 . We use our own numerical predictions for the LER dependence on the code distance

at a physical error rate $p_{\text{phys}} = 10^{-3}$, rather than the reference 10^{-4} . To ensure the noise is sufficiently suppressed, we identify the smallest code distance d such that the mean LEP per circuit satisfies $\mu_{N,d} \leq 10^{-2}$, and that is $d = 21$. To obtain a LEP distribution with the same mean as $(N_{\text{windows}}, d) = (1.38 \times 10^9, 19)$, we used $(N_{\text{windows}}, d) = (2.38 \times 10^5, 11)$.

We considered parameters $J = 16$ and $N = 5$ from Ref. [31, Sec. IV.B] (note the meaning of N here differs from the usual meaning of decoding window count used in this paper). Therefore, $N_{\text{values}} = 2JN = 160$ expectation values need to be estimated through different quantum circuits. Each circuit should be run M_0 times, which means that $N_{\text{values}}M_0 = 16000$ quantum circuit runs occur in total.

Appendix F: Code Distance Influence on Resources

The surface code qubit count scales quadratically with distance d , and the duration of each logical operation scales at most linearly with d . Therefore the spacetime volume increase is $(d_{\text{start}}/d_{\text{targ}})^3\omega - 1 \approx 21\%$, where ω is the multiplicative time cost defined in Eq. (D2).

Appendix G: DCS-QEM Performance Metrics

In Fig. G.1, we present an alternative performance metric for the data in Fig. 7; namely, the absolute mean bias:

$$\text{bias} := \left| \langle Z \rangle_{\text{th}} - \frac{1}{N_{\text{rep}}} \sum_{i=1}^{N_{\text{rep}}} \langle Z \rangle_i \right|, \quad (\text{G1})$$

which we call ‘Bias’ for short in the y-axis labels of panels (a,c). This metric does not account for variance, so we plot the latter in panels (b,d). In the limit of an infinite number of repetitions, the noiseless estimator bias drops to exactly zero.

Panels (a,c) show that MLE could achieve the target absolute mean bias (0.633×10^{-2}) for the application described in Section VI A without any time overhead.

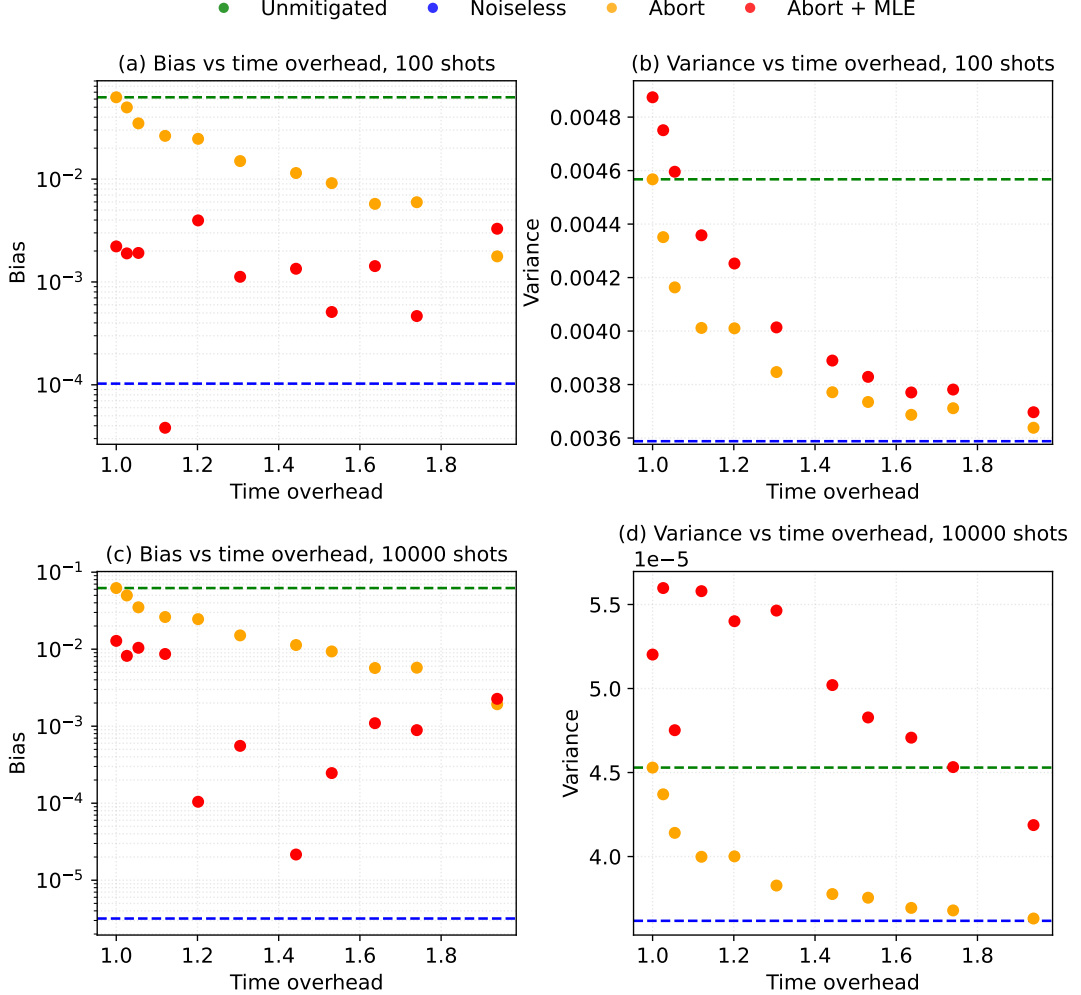


FIG. G.1. (a,c) The same data as in Fig. 7b,d but analysed using a different performance metric: the bias, defined in Eq. (G1). (b,d) The variance of the estimator output distributions.